Materiales de Construcción
Vol. 73, Issue 349, January-March 2023, e306
ISSN-L: 0465-2746
https://doi.org/10.3989/mc.2023.297022

Preparation of shrinkage-free alkali-activated slag material using MgO as both the activator and the expansive agent

P. Chen[a, b, c], Q. Chen[d], Y. Fang[d] ✉, C. Wang[a], X. Wang[a], J. Li[a], Y. Wang[a]

a. School of Civil Engineering and Architecture, Anhui University of Science and Technology, Huainan, (P.R. China)
b. Institute of Environment-friendly Materials and Occupational Health, Anhui University of Science and Technology, Wuhu, (P.R. China)
c. Anhui Hongchang New Material Co. Ltd, Huaibei, (P.R. China)
d. College of Mechanics and Materials, Hohai University, Nanjing, Jiangsu, (P.R. China)
✉: yfang20@crimson.ua.edu

Received 28 June 2022
Accepted 20 December 2022
Available on line 06 March 2023

ABSTRACT: Alkali-activated slag (AAS) materials activated by NaOH or waterglass has been long-term criticized for the developed substantial shrinkage. To this regard, this paper explored MgO as both an activator and an expansive agent to prepare shrinkage-free AAS. The setting time, mechanical strength, pore structure, autogenous shrinkage, drying shrinkage, and hydration products of MgO-activated AAS were studied. Experimental results confirmed that MgO can effectively mitigate the autogenous shrinkage and drying shrinkage of AAS via the expansive deformation caused by $Mg(OH)_2$. Generally, AAS with a higher dosage of MgO developed less shrinkages and refiner pore structures with more gel pores. An optimal dosage of 9% MgO is recommended to prepare AAS with near zero shrinkage and the highest flexural strength.

KEY WORDS: Alkali-activated slag; MgO; Autogenous shrinkage; Drying shrinkage.

Citation/Citar como: Chen, P.; Chen, Q.; Fang, Y.; Wang, C.; Wang, X.; Li, J.; Wang, Y. (2023) Preparation of shrinkage-free alkali-activated slag material using MgO as both the activator and the expansive agent. Mater. Construcc. 73 (349), e306. https://doi.org/10.3989/mc.2023.297022.

RESUMEN: *Preparación de materiales de retracción compensada empleando escoria activada alcalinamente utilizando MgO como activador y como agente expansivo.* Los materiales de escorias activadas alcalinamente (AAS) ya sea por NaOH o waterglass han sido criticados durante mucho tiempo por los problemas de retracción que estos sistemas presentan. A este respecto, este trabajo explora el empleo de MgO como activador y agente expansivo para preparar pastas de AAS sin retracción. Se estudiaron el tiempo de fraguado, la resistencia mecánica, la estructura de poros, la retracción autógena, la retracción por secado y los productos de hidratación de las pastas de AAS activadas con MgO. Los resultados experimentales confirmaron que el MgO puede mitigar eficazmente la retracción tanto autógena como por secado de los sistemas de AAS a través de la deformación expansiva causada por el $Mg(OH)_2$. En general, los AAS con una dosis más alta de MgO desarrollaron menos retracción y estructuras de poros más refinadas con más poros de gel. Se recomienda una dosis óptima del 9% de MgO para preparar AAS con una retracción cercana a cero y la mayor resistencia a la flexión.

PALABRAS CLAVE: Escoria activada con álcali; MgO; Retracción autógena; Retracción por secado.

1. INTRODUCTION

Concrete with ordinary Portland cement (OPC) is one of the most widely utilized artificial construction materials in the world (1). However, the concrete industry has a significant impact on the environment. The production of OPC accounts for about 7% of all anthropogenic greenhouse gas emissions worldwide (2-4). Considering the high CO_2 burden, sustainable alternative cements are in demand to improve the eco-efficiency of concrete and minimize the related carbon emissions. In recent years, alkali-activated slag (AAS) materials have attracted the most attention as a promising eco-friendly alternative to OPC-based binders (5). The key advantages of AAS include the reuse of industrial by-products, the reduction of waste material deposition, and the use of less additional energy during the clinkering process (6). Extensive studies confirm that AAS possess abundant superiorities like quick setting, high early-age strength, good durability, and good resistance to acid corrosion (7). In addition, it was shown that AAS-based materials release 25%-50% less CO_2 while saving 40% embodied energy compared with OPC (8-11).

However, AAS faces various obstacles as a construction material in practical engineering. One of the major issues is that AAS, which is normally activated by NaOH or water glass, experiences excessive shrinkage during the setting and hardening processes, resulting in cracking (12, 13). It was reported that the autogenous shrinkage of AAS can increase continuously during a 56-day recording period (4) and become about 5 times larger than that of OPC (14). In detail, the recorded autogenous shrinkage of AAS with various concentrations of activators (Na_2CO_3 or NaOH/water glass) can be as high as 1.5% or 3.5% at 28 d, respectively (15). Ye et al. (16) found that AAS experiences substantial drying shrinkage despite the exposed relative humidity. The maximum recorded value of drying shrinkage was as high as up to 10000 με. The shrinkages of AAS exclusively suggest that AAS suffers high risks of cracking and may be more easily invaded by substances (such as Cl^-, sulfates, or bacteria) during its service life. Therefore, there is an emerging need to mitigate the shrinkage of AAS for the broader application of these alternative binders (12, 17).

Considering the strategies of shrinkage mitigation, using an expansive agent seems a simple and possible option. Nevertheless, the efficiencies of these expansive agents should be examined when used in AAS to avoid unexpected reductions in strength and durability. Gao et al. (18) investigated the feasibilities of high-performance concrete expansion agents (HCSAs) and U-type sulfoaluminate-based expansion agents (UEAs) to mitigate the drying shrinkage of AAS. The drying shrinkage of AAS can be reduced by 51.9% to 62.8% by using HCSA or 38.4% by using UEA. However, the compressive strengths of AAS are reduced by about 10%. Hanjitsuwan et al. (19) tried to explore new admixtures as expansive agents for AAS by using flue gas desulfurization, gypsum, and dolomite. Experimental results showed the drying shrinkages of AAS are reduced by 20% with 5% expansive agents, indicating low shrinkage mitigation efficiencies. Ye et al. (16) claimed that gypsum can contribute to less shrinkage of AAS since it can promote the formation of expansive phases at an early age; nevertheless, the long-term final drying shrinkage was still prominent. Li et al. (20) reported that 10% CaO-based expansion agent can reduce the expansion rate of AAS by 20%. However, the 28d compressive strength was decreased by 22.5% with the addition of a CaO-based expansion agent. Notable, the expansive agents widely used in OPC systems may not work effectively in the AAS system (21-23); thus, new attempts are encouraged toward shrinkage-free AAS.

Recently, reactive MgO has been proposed as an activator for AAS, owing to its features of low cost and low noxiousness (24). Voet al. (25) found that 7.5% MgO was an optimal dosage for AAS to achieve the highest compressive strength. Hwang et al. (26) pointed out that a small amount of MgO can achieve significant strength development of AAS, which was attributed to the formation of hydrogarnet (Ht) and refinement of the porous matrix. Jin et al. (27) reported the correlation between the reactivity of MgO and compressive strength, which is that highly reactive MgO (reactivity <30s) results in higher early strength, while the highest 90d strength was achieved by those MgO with lower reactivities around 30–100s. Notably, MgO can be used as an expansive agent of AAS considering the transformation of MgO to $Mg(OH)_2$ can result in a 3-fold volume expansion (28-30).

Therefore, MgO may be used as both the activator and the expansive agent for AAS. The objective of this study is to evaluate the efficiency of MgO as both the activator and the expansive agent to mitigate the shrinkage of AAS. To that end, a comprehensive experiment program was carried out to gain a fundamental understanding of the underlying working mechanisms of the proposed shrinkage-free AAS. In particular, the effects of MgO content on the setting time, mechanical properties, autogenous shrinkage, drying shrinkage, pore structure, and hydration products of AAS will be investigated.

2. MATERIALS AND METHODS

2.1. Materials

In this study, ground granulated blast slag (GGBS) was provided by a local supplier with the grade S105

according to GB/T18046 (31) and the BET surface area of 1535 m^2/kg. The chemical composition of GGBS was obtained by X-ray fluorescence (XRF) (Rigaku Corporation), as shown in Table 1. The main chemical components are SiO_2, CaO and Al_2O_3 with little Fe_2O_3, MgO, TiO_2, and K_2O. The particle size distribution was determined by a Mastersizer 2000 (UK Malvern Instruments Co. LTD, Malvern, UK) laser particle size analyzer, as shown in Figure 1a. The D_{50} particle size of GGBS is about 20 μm. The mineral composition was analyzed by X-ray diffraction (XRD) technique using a Smart Lab X-ray diffractometer, as shown in Figure 1b. It can be seen that GGBS is vitreous with amorphous phases as its major content; and there also exists some melilite in GGBS.

Analytical reagent grade MgO was purchased from Tianjin Zhiyuan Chemical Reagent Co., LTD. According to DL/T 5296 (32), the activity of MgO was measured as follows: (1) 1.7g MgO was added into 200mL citric acid solution with a concentration of 1.3%; (2) phenolphthalein was added as the inductor to determine the time when the color of the solution turns into red. The activity index of MgO was measured as 75s, indicating the relatively high reactivity of MgO. Water without statement is tap water.

Table 1. Chemical composition of GGBS (wt. /%).

Component	SiO_2	CaO	Al_2O_3	Fe_2O_3	MgO	TiO_2	K_2O
GGBS	26.5	43.7	18.2	1.0	4.9	1.0	0.8

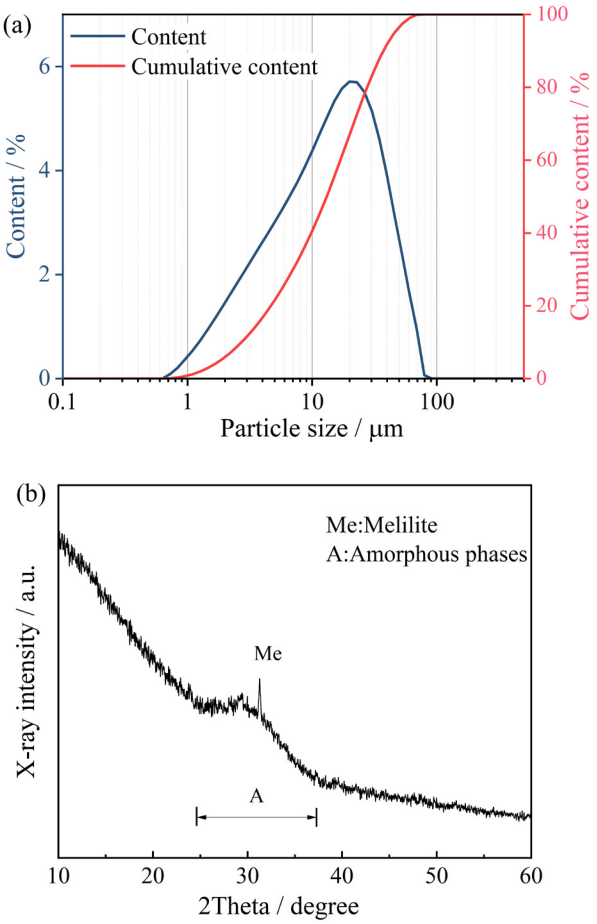

Figure 1. Particle size distribution (a) and XRD pattern (b) of GGBS.

2.2. Mix proportion

Five AAS mixtures were considered to prepare one-part MgO-activated slag material. The dosages of MgO were 3%, 6%, 9%, 12%, and 15% of mass of GGBS, as shown in Table 2. The mix ID "MS*x*" indicates the AAS was made with *x*% MgO activator by the weight of precursor (GGBS). The water/GGBS ratio of all mixtures was 0.48. To prepare the one-part AAS, the precursor materials and solid activators were dry-mixed for 5 mins, and then mixed another 5 mins after adding all the water. Samples with a size of 40 mm× 40 mm× 160 mm were prepared for the measurement of mechanical strength. The produced samples were cured at 23 °C and relative humidity higher than 95% until the designated test day.

Table 2. Mixing proportion of AAS (g).

Mixtures	GGBS	Water	MgO
MS3	67.57	32.43	2.03
MS6	67.57	32.43	4.06
MS9	67.57	32.43	6.09
MS12	67.57	32.43	8.12
MS15	67.57	32.43	10.15

2.3. Test methods

2.3.1. pH of pore solution

The pH of pore solution of AAS was measured by a PHS-2F pH meter. GGBS and MgO were firstly proportioned according to Table 2, and the ratio of deionized water/GGBS was 1.0 for all samples to avoid the quick setting of AAS to measure the 24h pH of pore solution. Then, the mixture was reelingly shaken by a shaker. The pore solution was filtered out using a 20 nm membrane.

2.3.2. Setting time

The setting time of AAS was measured using the Vicat method according to ASTM C191 (33). Fresh AAS was casted into a conical sample of designed size.

2.3.3 Autogenous shrinkage

The autogenous shrinkage of AAS was measured using the corrugated tubes with a length of 425 mm and a diameter of 28.5 mm in accordance with ASTM C1698 (34). Triplicate samples were measured for each mixture. A dilatometer bench with a dial gauge fixed on one end was used to measure the length changes of AAS from the final setting. The autogenous shrinkage of AAS can be calculated by the following Equation [1]:

$$\varepsilon_{\text{autogenous}} = \frac{L(t)-L(t_{\text{fs}})}{L(t_{\text{fs}})} \times 10^6 \frac{\mu\text{m}}{\text{m}} \qquad [1]$$

where $L_{(tfs)}$ is the initial length of the specimen measured after final setting, $L_{(t)}$ is the length of the specimen measured over time.

2.3.4. Drying shrinkage

The drying shrinkage of the AAS was tested according to ASTM C596 (35) using a prismatic specimen with a size of 25mm×25mm×280mm. Fresh AAS was first casted into the prismatic specimen and followed by 3d moist curing. Then, those specimens were transferred to the test chamber at a temperature of 23 ºC and a relative humidity of 60%. Triplicate samples were tested for each group. During the first 14d, drying shrinkage value was measured once a day and then measured separately at 28d, 35d, 42d, 49d and 56d. The drying shrinkage of AAS could be obtained according to Equation [2]:

$$\varepsilon_{drying} = \frac{\Delta L-\Delta L(t)}{L(0)} \times 10^6 \frac{\mu m}{m} \qquad [2]$$

where ΔL is the length difference between the initial length of the specimen and standard part; $\Delta L_{(t)}$ is the length difference between the specimen and standard part at age t; $L_{(0)}$ is the initial length of the specimen (280mm).

2.3.5. Mechanical strength

The compressive strengths of the produced samples were measured by a DYE-300 compressive strength testing machine with a loading rate of 1 KN/s according to ASTM C349 (36). The flexural strength was tested with a loading rate of 0.01 mm/min with Testometric X500-50 machine according to ASTM C348 (37). Triplicate samples were tested at the ages of 3d, 7d, and 28d. Average strengths were reported.

2.3.6. Nuclear magnetic resonance test (NMR)

A MesoMR23-060V-1NMR instrument with a resonance frequency of 21.3 MHz was used to analyze the pore structure of AAS at 28d. Before the testing, all the samples were vacuum saturated by a BSJ fully automatic saturation machine.

2.3.7. X-ray diffraction (XRD)

XRD was used to evaluate the mineral composition of hydration products in produced MgO-activated slag materials. The samples were scanned using a Smartlab SE X-ray diffractometer from 5° to 70° at a scanning speed of 5°/min with Cu source (40 kV, 50 mA). At 7d and 28d, all the specimens were crushed in a sealed bag and then soaked in anhydrous ethanol to entirely stop the reaction. After 7d soaking, the samples were taken out and dried in a vacuum chamber. Then the specimens were crushed and ground into fine powders, and the particles size less than 0.075mm were sieved out via #200 meshes for examination.

3. RESULTS AND DISCUSSION

3.1. pH of pore solution

Figure 2 shows the pH of the pore solution of AAS over 24 h. It clearly shows that the pH of pore solution is generally higher in AAS, with more MgO at each time. A longer age facilitated the increment in the pH of the pore solution. The hydration of the AAS activated by MgO began with the hydration of MgO to form $Mg(OH)_2$, which is the activator for GGBS. The presence of $Mg(OH)_2$ is a competing result of the formation and consumption of $Mg(OH)_2$. Then, a higher dosage of MgO implies that more MgO is available for forming $Mg(OH)_2$, resulting in a higher pH pore solution.

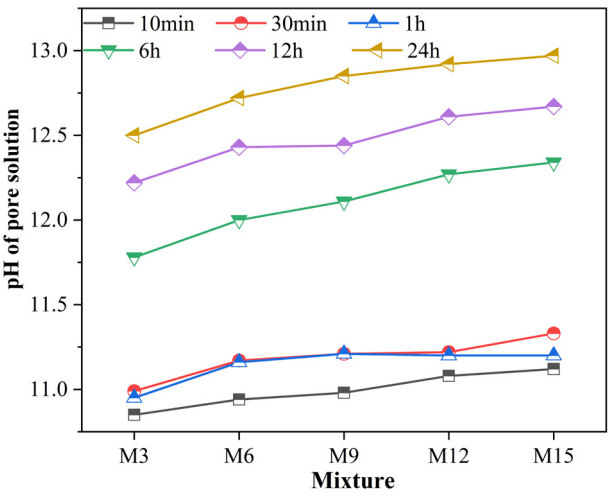

Figure 2. pH of the pore solution of AAS.

3.2. Setting time

Figure 3 presents the initial and final setting times of AAS with various dosages of MgO. With the increase

of MgO, the hydration process of AAS was accelerated, as indicated by the reduction of the initial and final setting times. Compared with MS3, the initial setting times of MS6, MS9, MS12, and MS15 were decreased by 21.7%, 33.9%, 37.8%, and 44.3%, respectively, and the final setting times were accordingly decreased by 18.5%, 36.3%, 39.6%, and 41.5%, respectively. Additionally, saturated dosages of MgO seem to be determined at the MgO level between 12% and 15% since the final setting times of groups MS12 and MS15 reach at similar value. The activation mechanism of GGBS by MgO involves the following process. Highly reactive MgO reacts with water, producing a significant amount of expansive alkaline $Mg(OH)_2$. Alkali hydration of a GGBS corresponds to a complex process including the initial dissolution of the glass phase in the GGBS and consequent a later precipitation of the hydration products (C-A-S-H). Similar to the other pozzolans, the rate of dissolution of the glass in GGBS increases at a higher pH value. For the limited mixing water, excessive MgO could not generate a higher pH value due to the saturation of alkali compounds in the pore solutions. As a result, the dissolution of GGBS was slowed down, resulting in a similar hydration degree of GGBS, as indicated by the similar value of the final setting time of MS15 and MS12.

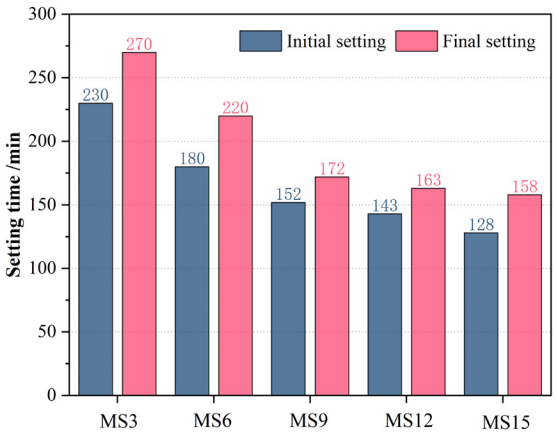

Figure 3. Setting time of AAS with various dosages of MgO.

3.3. Mechanical strength

Figure 4 presents the average compressive strength of AAS activated by MgO at different curing ages along with the standard errors. As can be seen from this figure, the average compressive strengths of MS3 at 3d and 7d are less than 10 MPa. Compared with MS3, the 3d average compressive strengths of MS6, MS9, MS12, and MS15 were improved by 73.6%, 105.5%, 136.8%, and 131.1%, respectively. When the curing age went to 28d, the average compressive strengths of MS6, MS9, MS12, and MS15 were enhanced by 6.9%, 37.1%, 41.4%, and 30.8%, respectively compared with MS3. Additionally, MS12 achieved the highest average compressive strengths at all ages, with 136.8%, 80.4%, and 41.4% increments in the average compressive strength at 3d, 7d, and 28d, respectively, compared with MS3. More MgO can be expected to produce more hydrated $Mg(OH)_2$, bringing more alkali compounds into the AAS pore solution. In this manner, the hydrolysis of Al–O–Si bonds can be facilitated by more OH^- group, leading to the quicker breakdown of the depolymerized glass network and fast release of Si and Al ion in the pore solution. As a result, the hydration degree of GGBS and the formation of hydration products were promoted, contributing to higher average compressive strength. However, when the content of MgO was raised to 15%, AAS may suffer from excessive expansive stress and deformation due to more expansive hydration products like $Mg(OH)_2$ generated in the mixture, resulting in more microcracks in the mixtures and lower average compressive strength.

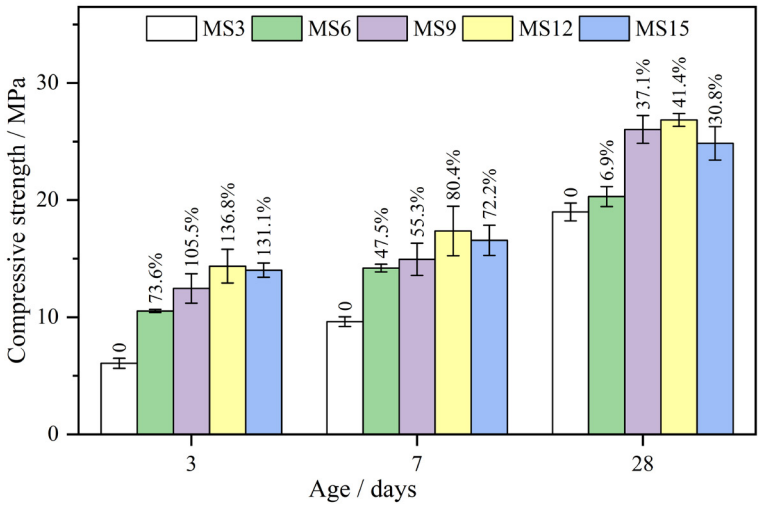

Figure 4. Average compressive strength of AAS activated by MgO.

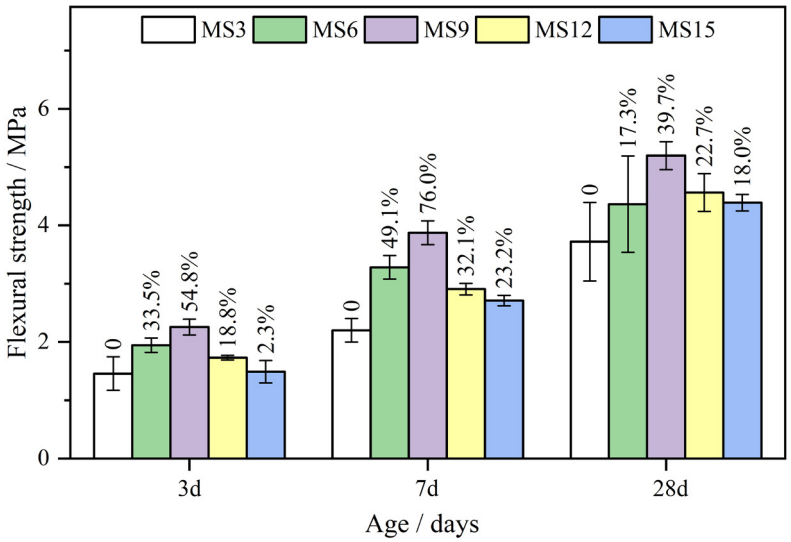

Figure 5. Average flexural strength of AAS activated by MgO.

Beyond the average compressive strength, the average flexural strength development of AAS was also explored to fully evaluate the influence of MgO on the mechanical strength of AAS, as shown in Figure 5. The optimum content for the highest average flexural strength was slightly different compared to that for average compressive strength, which was given in MS9. More specifically, compared with MS3, MS9 had 54.8%, 76.0%, and 39.7% increments in average compressive strength at 3d, 7d, and 28d, respectively. The difference between the average compressive strength and average flexural strength might be caused by the sensitivity of expansion and shrinkage deformation in these two tests, considering flexural strength is more sensitive to micro-cracks in samples. In summary, 9% was confirmed as the final optimal dosage for AAS activated by using MgO as the single activator.

3.4. Pore structure

The pore structure of AAS at 28d was measured using NMR, as shown in Figure 6a. The pore structure is dramatically refined by the increase in MgO, leading to the reduction of the total pore volume and the shift towards finer pores. The improvements in pore structure can be attributed to more expansive hydration products and the higher hydration degree of GGBS. To quantitatively analyze the pore structure, the pore sizes were divided into four zones: Z1 (<20nm), Z2 (20 – 100nm), Z3 (100 – 200nm), and Z4 (>200nm). The obtained result is concluded in Figure 6b. Normally, the pores in Z1 are related to gel pores in the hydration product. In other words, the volume of pores less than 20 nm can be regarded as an index of AAS's hydration degree. In this study, the pore volumes located in zone Z1 increased with the increase of MgO, implying that the increase of MgO can promote the hydration degree of GGBS. In addition, the pores located in Z2 decreased with the content of MgO increasing, which can be attributed to the expansive hydration and denser microstructure caused by a higher hydration degree. This is well consistent with the results of mechanical strength, as shown in Figure 4 and Figure 5.

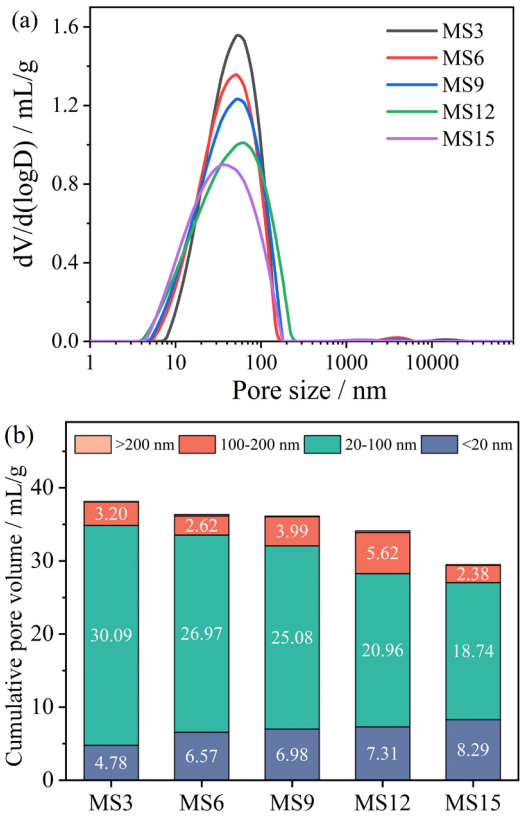

Figure 6. Pore size distribution of 28d AAS samples (a) and pore structure analysis (b).

Especially, the correlation between the pore volumes and MgO content could be linearly fitted for zones Z1 and Z2, as shown in Figure 7. It can be found that the gel pores (less than 20 nm) in the hydration products of AAS increase linearly (R^2 = 0.905) with the content of activators, while the capillary pores between 20-100 nm decrease linearly (R^2 = 0.989) with the amount of MgO. This indicates that the amount of expansive hydration products generated by MgO is the key factor in the refinement of pore structures. These expansive alkali compounds involved in hydration effectively fill the pores and refine the pore structure, which is the direct reason for the improvement of the compressive strength of AAS within a certain range.

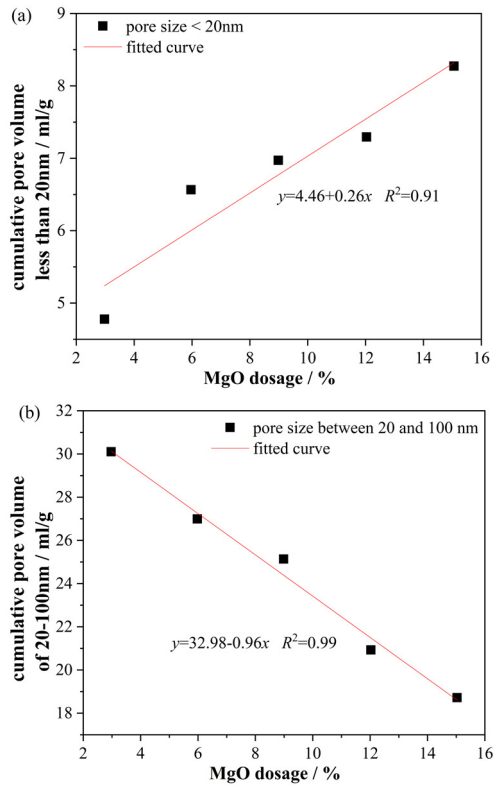

Figure 7. Linear approximations of cumulative pore volume and pore size: (a) pore size<20nm; (b) pore size ranging from 20nm to 100nm.

3.5. Hydration products analyzed XRD

Figure 8 shows the XRD patterns of MgO-activated slag pastes at the ages 7d and 28d. Major crystalline minerals found in the pastes include typical hydration products such as hydrogarnet (Ht), C-A-S-H, gehlenite, MgO, and $Mg(OH)_2$, identified according to references and their JCDPF files (38-41). All samples of AAS possess similar phase compositions. With the increase of MgO, more $Mg(OH)_2$ appears to be present in AAS pastes. Nevertheless, no other apparent differences can be found among AAS mixtures at different ages.

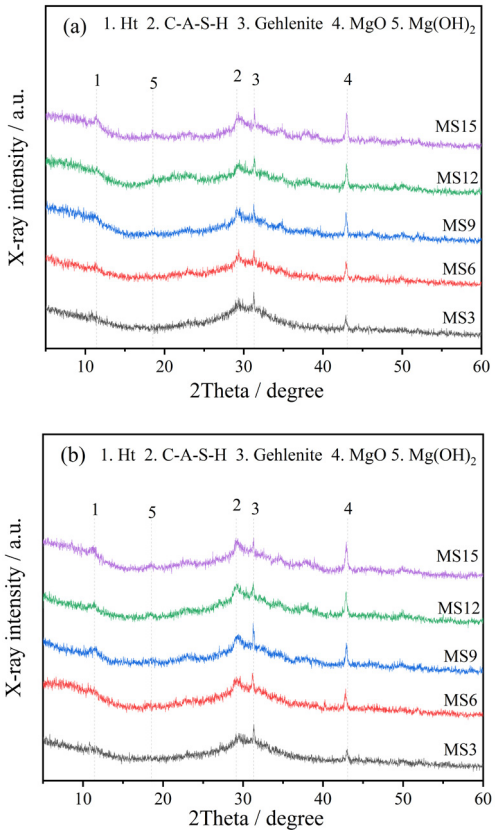

Figure 8. XRD patterns of AAS at 7d (a) and 28d (b).

3.6. Autogenous shrinkage

Figure 9 shows the results of autogenous shrinkage of five AAS mixtures over 56d. The development of autogenous shrinkage of AAS can be generally classified into three stages based on the tendency as marked in the figure. The first stage is located between the final setting and about 4d. Most of the AAS mixtures developed substantial expansive deformations during that stage. For MS3 with the lowest MgO dosage, its deformation during the first stage is immeasurable, indicating a low activated degree of GGBS due to insufficient activator. During stage I, the expansive deformations of AAS except for MS3 developed in almost linear tendencies with the curing age. In addition, the expansive deformation was sensitive to the content of MgO. With the higher dosage of MgO, there were higher expansive deformations in the mixtures. As a result, the highest autogenous expansion was recorded at 1713.5 με in MS15. Unlike traditional AAS activated by NaOH or water glass, which develops excessive autogenous shrinkage from the beginning of the final setting. The expansive properties of AAS activated by MgO can be attributed to the following two mechanisms. During the setting and hardening processes of AAS, the hydration heat released from the activation of GGBS induces the first part of expansive

deformation. However, this part of expansive deformation lasts for short periods due to the quick setting of AAS (< 4 hours). The predominant mechanism for the expansion is exclusively the expansive nature of the hydration of MgO. During the dissolution process of MgO-activated slag, MgO could react with water and cause the formation of $Mg(OH)_2$. This part of the reaction produces high alkaline conditions for activating GGBS and contributes to expansive $Mg(OH)_2$. Ye et al. (28) determined that during the transformation of MgO into $Mg(OH)_2$, the bulk volume of material could be increased at least by 2 times.

After this initial period, autogenous shrinkage became more obvious since the dissolution of MgO almost finished in Stage I. The length of the MgO-activated slag started to reduce, and Stage II occurred. As shown in Figure 9, the autogenous expansion of AAS decreased quickly in about 10 days, despite the dosage of MgO. Compared with Portland cement, AAS normally possesses finer and denser pore structures, which inevitably cause high autogenous shrinkage due to the high pore pressure. Besides the self-desiccation of AAS, the consumption of ions during hydration also induces shrinkage. For the MgO-activated slag, another mechanism for the chemical shrinkage would be the consumption of the expansive $Mg(OH)_2$.

Stage III occurred in around 14 days, which could be assumed as a steady period of MgO-activated slag. In this period, the deformation of AAS tends to be stable except for low dosages such as MS3 and MS6. This can be attributed to the benefit of expansive $Mg(OH)_2$. Especially, the final shrinkage of the group MS9 almost reached zero. In the contrast, for AAS with lower dosages of MgO (MS3 and MS6), the autogenous shrinkage continuously developed over time. As a result, the final deformations were recorded as -1546.4με and -1138.1με for MS3 and MS6, respectively.

3.7. Drying shrinkage

Figure 10 shows the drying shrinkage of AAS activated by MgO over 56d. As shown in the figure, the addition of MgO could also significantly mitigate the drying shrinkage of AAS. In addition to the low dosage of MgO like in MS3, the drying shrinkage developed continuously to 2700με at 56d. The drying shrinkage of AAS was significantly altered when the activator MgO is used with more than 9 wt.% of precursors, with little drying shrinkage in the mixtures for the group MS9, while MS12 and MS15were even in expansive conditions at 56d, indicating that AAS shrinkage can be efficiently controlled by MgO activation. Considering the autogenous shrinkage of AAS shown in Figure 9, MS9 might be the optimum group to achieve zero shrinkage including autogenous and drying for the application of alkali-activated slag.

It has been reported that the large drying shrinkage in AAS is caused by the structural incorporation of alkali cations in C-A-S-H. As a result, the stacking regularity of C-A-S-H layers is reduced, causing the C-A-S-H easier to collapse and redistribute during the drying process (16, 38). A slight expansion is expected for an engineered AAS for practical application. The benefits of MgO on drying shrinkage mitigation can be summarized in two aspects. Firstly, the formation of expansive hydration products of $Mg(OH)_2$ contributes to the major expansive values. Secondly, with the increased amount of MgO, there are more alkali compounds to accelerate the dissolution of GGBS, thus increasing the hydration degree of the slag and generating more hydration products. As a result, there is a denser microstructure in the AAS mixtures activated by a high amount of MgO, which will reduce moisture losses during the drying process. This can be confirmed by the water loss during the drying process until 56d, as shown in Figure 11.

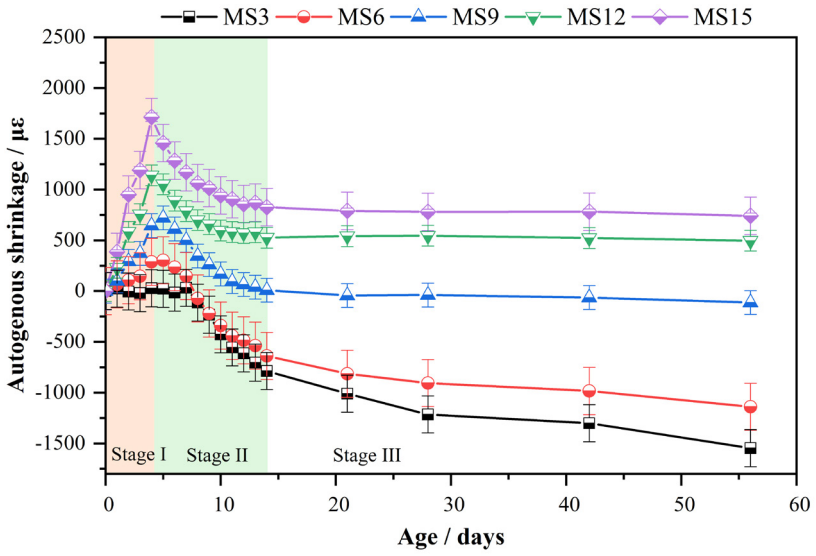

Figure 9. Autogenous shrinkage of AAS over curing time.

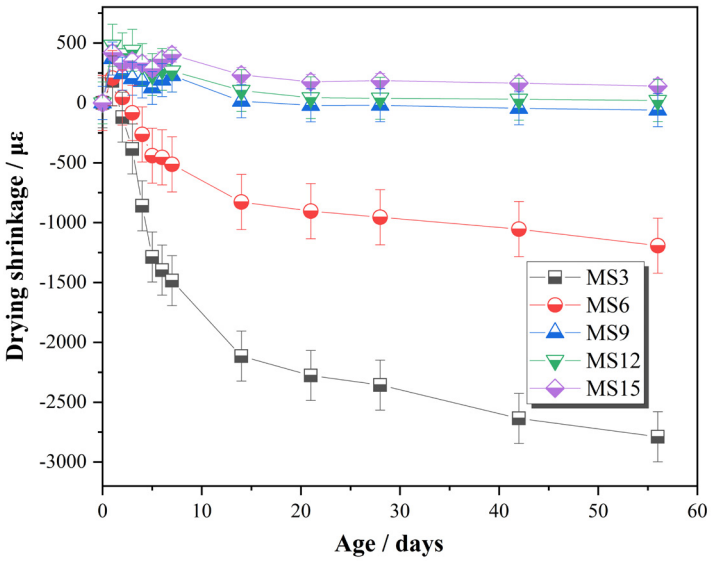

Figure 10. Drying shrinkage of AAS over the curing time.

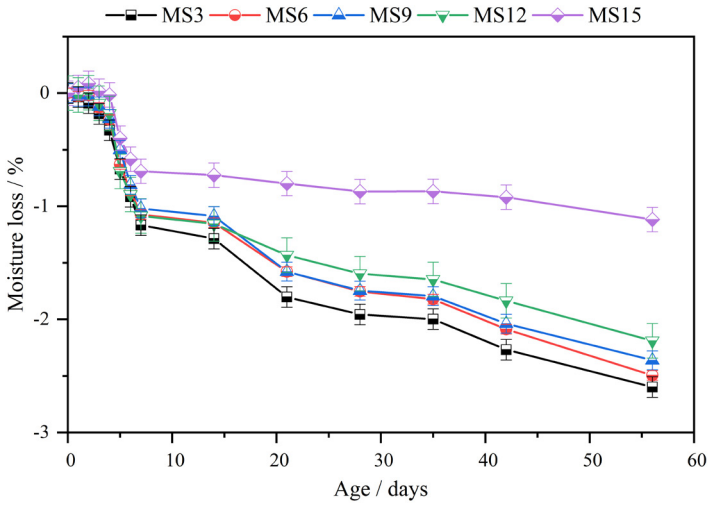

Figure 11. Moisture loss of AAS over time.

It can be found that AAS lost most of its moisture during the first week, regardless of MgO content. After 7d, the moisture in the samples with a higher amount of MgO reduced slower compared with MS3, possibly because the AAS activated by higher dosages of MgO developed a denser microstructure, as indicated by the pore structure analysis. In addition, the presence of hydrophilic, un-hydrated MgO may also be beneficial to retain moisture during the drying process.

4. CONCLUSIONS

This study investigated the feasibility of MgO as both an activator and an expansive agent for AAS to mitigate excessive shrinkage. Experimental results confirmed that one-part AAS can be prepared by using MgO as the activator. With the increase of the activator MgO, the hydration process of GGBS was accelerated, as indicated by the reduction of the initial and final setting times. More importantly, MgO can effectively mitigate the autogenous shrinkage and drying shrinkage of AAS via the expansive deformation caused by $Mg(OH)_2$. In addition, the compressive and flexural strengths of AAS increase with the content of MgO until reaching 15% MgO and 12% MgO, respectively, for all curing ages, because the high content of MgO provides quicker dissolution of the glass phase in GGBS and a more expansive alkali, thus mitigating shrinkage deformation and inducing fewer micro-cracks. In contrast, excess MgO causes large expansive deformation, compromising mechanical properties. The pore structure is refined by the increase of MgO, as indicated by the increase of gel

pores less than 20 nm and the decrease of capillary pores between 20 nm and 100 nm. It's observed that 9% of MgO can achieve the optimum effect as a solid activator and an expansive agent for AAS, which can reach near zero shrinkage from 14d and obtain the highest mechanical properties.

ACKNOWLEDGEMENTS

This study was funded by Key Project of Natural Science Research in Universities of Anhui Province (KJ2020ZD33), National Natural Science Foundation of China (52008003), Research Foundation of the Institute of Environment-friendly Materials and Occupational Health (Wuhu), Anhui University of Science and Technology (ALW2020YF16), Special Project on Science and Technology of Anhui Province (202003a07020023), Anhui Province Science and Technology Plan Project of Housing Urban-Rural Construction(2020-YF12).

AUTHOR CONTRIBUTIONS:

Conceptualization: Y. Fang. Formal analysis: Q. Chen. Funding acquisition: P. Chen. Investigation: P. Chen, Q. Chen, C. Wang, X. Wang, J. Li, Y. Wang. Methodology: P. Chen. Supervision: Y. Fang. Writing, original draft: P. Chen. Writing, review & editing: Y. Fang.

REFERENCES

1. Fang, Y.; Wang, J.; Qian, X.; Wang, L.; Chen, P.; Qiao, P. (2022) A renewable admixture to enhance the performance of cement mortars through a pre-hydration method. *J. Clean. Prod.* 332, 130095. https://doi.org/10.1016/j.jclepro.2021.130095.
2. Xu, D.; Cui, Y.; Li, H.; Yang, K.; Xu, W.; Chen, Y. (2015) On the future of Chinese cement industry. *Cem. Concr. Res*. 78, 2-13. https://doi.org/10.1016/j.cemconres.2015.06.012.
3. Zhang, C.Y.; Han, R.; Yu, B.; Wei, Y.M. (2018) Accounting process-related CO_2 emissions from global cement production under Shared Socioeconomic Pathways. *J. Clean. Prod*. 184, 451-465. https://doi.org/10.1016/j.jclepro.2018.02.284.
4. Chen, P.; Wang, J.; Wang, L.; Xu, Y. (2019) Perforated cenospheres: A reactive internal curing agent for alkali activated slag mortars. *Cem. Concr. Compos*. 104, 103351. https://doi.org/10.1016/j.cemconcomp.2019.103351.
5. Roy, D.M. (1999) Alkali-activated cements opportunities and challenges. *Cem. Concr. Res*. 29 [2], 249-254. https://doi.org/10.1016/S0008-8846(98)00093-3.
6. Ye, H.; Radlińska, A. (2017) Shrinkage mitigation strategies in alkali-activated slag. *Cem. Concr. Res*. 101, 131-143. https://doi.org/10.1016/j.cemconres.2017.08.025.
7. Shi, C.; Roy, D.; Krivenko, P. (2003) Alkali-activated cements and concretes. *CRC press*. https://doi.org/10.1201/9781482266900.
8. Karozou, A.; Konopisi, S.; Paulidou, E.; Stefanidou, M. (2019) Alkali activated clay mortars with different activators. *Constr. Build. Mater.* 212, 85-91. https://doi.org/10.1016/j.conbuildmat.2019.03.244.
9. Gonçalves, M.; Vilarinho, I.S.; Capela, M.; Caetano, A.; Novais, R.M.; Labrincha, J.A.; Seabra, M.P. (2021) Waste-based one-part alkali activated materials. *Mater.* 14 [11], 2911. https://doi.org/10.3390/ma14112911.
10. Rodríguez, E.; Bernal, S.; De Gutiérrez, R.M.; Puertas, F. (2008) Alternative concrete based on alkali-activated slag. *Mater. Construcc.* 58 [291], 53-67. https://doi.org/10.3989/mc.2008.v58.i291.104.
11. Alcaide, J.; Alcocel, E.G.; Puertas, F.; Lapuente, R.; Garcés, P. (2007) Carbon fibre-reinforced, alkali-activated slag mortars. *Mater. Construcc.* 57 [288], 33-48. https://doi.org/10.3989/mc.2007.v57.i288.63.
12. Palomo, A.; Grutzeck, M.; Blanco, M. (1999) Alkali-activated fly ashes: A cement for the future. *Cem. Concr. Res*. 29 [8], 1323-1329. https://doi.org/10.1016/S0008-8846(98)00243-9.
13. Puertas, F.; Gil-Maroto, A.; Palacios, M.; Amat, T. (2006) Alkali-activated slag mortars reinforced with AR glassfibre. Performance and properties. *Mater. Construcc.* 56 [283], 79-90. https://doi.org/10.3989/mc.2006.v56.i283.10.
14. Kumarappa, D.B.; Peethamparan, S.; Ngami, M. (2018) Autogenous shrinkage of alkali activated slag mortars: Basic mechanisms and mitigation methods. *Cem. Concr. Res*.109, 1-9. https://doi.org/10.1016/j.cemconres.2018.04.004.
15. Sakulich, A.R.; Bentz, D.P. (2013) Mitigation of autogenous shrinkage in alkali activated slag mortars by internal curing. *Mater. Struct.* 46 [8], 1355-1367. https://doi.org/10.1617/s11527-012-9978-z.
16. Ye, H.; Radlińska, A. (2016) Shrinkage mechanisms of alkali-activated slag. *Cem. Concr. Res*. 88, 126-135. https://doi.org/10.1016/j.cemconres.2016.07.001.
17. Alonso, M.; Rodríguez, A.; Puertas, F. (2018) Viability of the use of construction and demolition waste aggregates in alkali-activated mortars. *Mater. Construcc.* 68 [331], e164-e164. https://doi.org/10.3989/mc.2018.07417.
18. Gao, X.; Liu, C.; Shui, Z.; Yu, R. (2021) Effects of expansive additives on the shrinkage behavior of coal gangue based alkali activated materials. *Crystals*. 11 [7], 816. https://doi.org/10.3390/cryst11070816.
19. Hanjitsuwan, S.; Injorhor, B.; Phoo-ngernkham, T.; Damrongwiriyanupap, N.; Li, L-Y.; Sukontasukkul, P.; Chindaprasirt, P. (2020) Drying shrinkage, strength and microstructure of alkali-activated high-calcium fly ash using FGD-gypsum and dolomite as expansive additive. *Cem. Concr. Compos*. 114, 103760. https://doi.org/10.1016/j.cemconcomp.2020.103760.
20. Shuang, L.; Zhi-lu, Z.; De-sha, T.; Wen-cong, H.; Linwen, Y.; Kai, Y. (2018) Investigation of the effect of CaO expansive agent on the restricted expansion rate of alkali activated slag mortar. *Bull. Chin. Ceram. Soc.* 37 [5], 1747-1752. (in Chinese)
21. Habert, G.; De Lacaillerie, J.D.E.; Roussel, N. (2011) An environmental evaluation of geopolymer based concrete production: reviewing current research trends. *J. Clean. Prod*. 19 [11], 1229-1238. https://doi.org/10.1016/j.jclepro.2011.03.012.
22. Rees, C.A.; Provis, J.L.; Lukey, G.C.; Van Deventer, J.S. (2008) The mechanism of geopolymer gel formation investigated through seeded nucleation. *Colloid Surf. A-Physicochem. Eng. Asp. A.* 318 [1-3], 97-105. https://doi.org/10.1016/j.colsurfa.2007.12.019.
23. Criado, M.; Palomo, A.; Fernández-Jiménez, A.; Banfill, P. (2009) Alkali activated fly ash: effect of admixtures on paste rheology. *Rheol. Acta.* 48 [4], 447-455. https://doi.org/10.1007/s00397-008-0345-5.
24. Jin, F.; Gu, K.; Al-Tabbaa, A. (2014) Strength and drying shrinkage of reactive MgO modified alkali-activated slag paste. *Constr. Build. Mater.* 51, 395-404. https://doi.org/10.1016/j.conbuildmat.2013.10.081.
25. Vo, D.H.; Hwang, C.L.; Yehualaw, M.D.; Liao, M.C. (2021) The influence of MgO addition on the performance of alkali-activated materials with slag− rice husk ash blending. *J. Build. Eng.* 33, 101605. https://doi.org/10.1016/j.jobe.2020.101605.
26. Hwang, C.L.; Vo, D.H.; Tran, V.A.; Yehualaw, M.D. (2018) Effect of high MgO content on the performance of alkali-activated fine slag under water and air curing conditions. *Constr. Build. Mater.* 186, 503-513. https://doi.org/10.1016/j.conbuildmat.2018.07.129.
27. Jin, F.; Gu, K.; Abdollahzadeh, A.; Al-Tabbaa, A. (2015) Effects of different reactive MgOs on the hydration of MgO-activated GGBS paste. *J. Mater. Civil. Eng.* 27 [7], B4014001. https://doi.org/10.1061/(ASCE)MT.1943-5533.0001009.
28. Ye, Q.; Yu, K.; Zhang, Z. (2015) Expansion of ordinary Portland cement paste varied with nano-MgO. *Constr.*

Build. Mater. 78, 189-193. https://doi.org/10.1016/j.conbuildmat.2014.12.113.
29. He, J.; Zheng, W.; Bai, W.; Hu, T.; He, J.; Song, X. (2021) Effect of reactive MgO on hydration and properties of alkali-activated slag pastes with different activators. *Constr. Build. Mater.* 271, 121608. https://doi.org/10.1016/j.conbuildmat.2020.121608.
30. Mo, L.; Deng, M.; Tang, M.; Al-Tabbaa, A. (2014) MgO expansive cement and concrete in China: Past, present and future. *Cem. Concr. Res*. 57, 1-12. https://doi.org/10.1016/j.cemconres.2013.12.007.
31. GB/T18046. (2017) Ground granulated blast furnace slag used for cement, mortar and concrete. Standardization Admination of the Peoples's Republic of China, China. (in Chinese).
32. DL/T 5296. (2013) Technical specification of magnesium oxide expansive for use in hydraulic concrete. National Energy Administration, China. (in Chinese).
33. ASTM C191. (2021) Standard test methods for time of setting of hydraulic cement by vicat needle. ASTM International, West Conshohocken, PA. https://doi.org/10.1520/C0191-21.
34. ASTM C1698. (2019) Standard test method for autogenous strain of cement paste and mortar. ASTM International, West Conshohocken, PA. https://doi.org/10.1520/C1698-19.
35. ASTM C596. (2018) Standard test method for drying shrinkage of mortar containing hydraulic cement. ASTM International,West Conshohocken, PA. https://doi.org/10.1520/C0596-18.
36. ASTM C349. (2018) Standard test method for compressive strength of hydraulic-cement mortars (using portions of prisms broken in flexure). ASTM International, West Conshohocken, PA. https://doi.org/10.1520/C0349-18.
37. ASTM C348. (2021) Standard test method for flexural strength of hydraulic-cement mortars. ASTM International, West Conshohocken, PA. https://doi.org/10.1520/C0348-21.
38. Suescum-Morales, D.; Bravo, M.; Silva, R.V.; Jiménez, J.R.; Fernandez-Rodriguez, J.M.; Brito, J. de (2022) Effect of reactive magnesium oxide in alkali-activated fly ash mortars exposed to accelerated CO_2 curing. *Constr. Build. Mater*. 342, 127999. https://doi.org/10.1016/j.conbuildmat.2022.127999.
39. Zhang, J.; Lv, T.; Han, Q.; Zhu, Y.; Hou, D.; Dong, B. (2022) Effects of fly ash on MgO-based shrinkage-compensating cement: microstructure and properties. *Constr. Build. Mater.* 339, 127648. https://doi.org/10.1016/j.conbuildmat.2022.127648.
40. Kuenzel, C.; Zhang, F.; Ferrandiz-Mas, V.; Cheeseman, C.; Gartner, E. (2018) The mechanism of hydration of MgO-hydromagnesite blends. *Cem. Concr. Res*. 103, 123-129. https://doi.org/10.1016/j.cemconres.2017.10.003.
41. Rodríguez-Navarro, C.; Hansen, E.; Ginell, W.S. (1998) Calcium hydroxide crystal evolution upon aging of lime putty. *J. Am. Ceram. Soc.* 81 [11], 3032-3034. https://doi.org/10.1111/j.1151-2916.1998.tb02735.x.